



Effect of nickel oxide additive on smelting mechanism of chromium-bearing vanadium titanomagnetite pellets

Gong-jin CHENG, Wei-dong TANG, Xiang-xin XUE

School of Metallurgy, Northeastern University, Shenyang 110819, China

Received 27 August 2020; accepted 8 April 2021

Abstract: The effect of nickel oxide additive on the smelting behaviors of chromium-bearing vanadium titanomagnetite pellets (CVTP) was investigated while analyzing the transfer behavior of nickel in iron and slag. The results show that when NiO added to CVTP increases from 0 to 6 wt.%, softening start temperature increases from 1148 to 1212 °C, and the softening end temperature increases from 1280 to 1334 °C; the melting start temperature increases from 1318 to 1377 °C, and the dripping temperature decreases from 1558 to 1521 °C. The pig iron comprises a compound of Fe–Ni–C. The slag structure depolymerizes with increasing nickel addition. The softening-melting behaviors of CVTP, the reduction of nickel into pig iron, and the depolymerization of slag structure indicate the feasibility of producing nickel–iron alloy through the blast furnace process.

Key words: nickel–iron alloy; chromium-bearing vanadium titanomagnetite pellets; smelting mechanism; slag structure

1 Introduction

Nickel is a crucial industrial metal, which has various uses, including as metallic material, electroplating material, catalyst in the hydrogenation of petrochemicals, battery material, pigments, dyes, ceramics, and other new materials. The consumption of nickel in the world increases yearly and especially in China. Nickel is mainly used in the production of stainless steel. The chromium-bearing vanadium titanomagnetite (CVTM) found in the Panzhihua area of Sichuan China is an abundant resource, with reserves of more than 3.5 billion tons. The CVTM contains iron, titanium, vanadium, chromium, and many other elements such as nickel and cobalt [1,2].

The production methods of nickel pig iron mainly include BF smelting, rotary Kiln-electric furnace (RKEF) smelting, and the Krupp–Renn process. To manufacture Fe–Ni alloy, the saprolite

laterite ore is disposed through the globally predominant RKEF smelting method [3]. The Krupp–Renn process is another way to produce sponge iron or Fe–Ni luppen for the production of stainless steel [4,5]. ELLIOTT et al [6] prepared the Fe–Ni particle through carbothermic reduction of a limonitic laterite ore. Hydrated ore such as nickel laterite ore (NLO) is difficult to utilize for its low iron grade and high silica content. LI et al [7] found that the solid-state reduction of NLO, and the high temperature, more time, and high content of CO and carbon were beneficial to the reduction rate of NLO. ZHU et al [8,9] examined the reduction of limonitic nickel laterite to produce Fe–Ni alloy. First, the optimum nickel laterite sinter was investigated through sinter pot test. Then, the nickel laterite sinter was reduced by the selective reduction-magnetic separation process, and the nickel content in Fe–Ni alloy was 12%. The recovery rate of nickel reached 85% through the selective reduction-magnetic separation process.

Corresponding author: Wei-dong TANG, E-mail: twdking@163.com;

Xiang-xin XUE, Tel: +86-24-83681711, E-mail: xuexx@mail.neu.edu.cn

DOI: 10.1016/S1003-6326(21)65670-4

1003-6326/© 2021 The Nonferrous Metals Society of China. Published by Elsevier Ltd & Science Press

RAO et al [10] studied the carbothermic reduction of nickel laterite ore for Fe–Ni alloy at low-temperature followed by magnetic separation. The Fe–Ni alloy is a low-cost raw material for stainless steel, and it is a suitable substitute for electrolytic nickel. ZHOU et al [11] studied the reduction of high-Mg low-Ni ore through magnetic separation to gather ferronickel concentrate. With the addition of NaCl, the Fe–Ni alloy particle grew in reduction process. LIU et al [12] studied the inhibition mechanism of selective reduction of nickel laterite ore with FeS. In the reduction process, the FeO content increases and reduction of iron is inhibited due to the generation of FeS and Na₂S. TIAN et al [13] studied the reduction of low-grade saprolite laterite with limoniticlaterite ore to enhance beneficiation of nickel and iron through thermodynamics calculation and mineralogical study. The main reduction mechanism of saprolite laterite is the transformation from Ni₂SiO₄ to NiFe₂O₄. LI et al [14] researched the carbothermic reduction of nickel slag through addition of CaCO₃. With the increasing addition of CaCO₃, the reduction degree of nickel slag increases, and the temperature reaching the maximum reduction rate decreases due to the decreasing content of FeSiO₃ in slag and improving the reduction conditions of iron oxides. YUAN et al [15] studied the enrichment of nickel and iron from nickel laterite ore through a deep reduction–magnetic separation method. The slag basicity is the main factor to affect the spilling and enriching rate of Fe–Ni alloy particles. Then, the Fe–Ni alloy particles can be effectively separated from gangue minerals by magnetic separation. However, the main utilization of nickel laterite ore focuses on the process of low temperature reduction and magnetic separation. This seems to require a faster and more efficient smelting method to utilize the nickel laterite ore and product Fe–Ni alloy. As the nickel gathers mainly in molten iron in the smelting process of CVTM in the blast furnace (BF), the effect of nickel on the pellet property and smelting process of CVTM

should be studied, which is also beneficial for further improving and perfecting the systematic investigation of valuable elements on reduction and smelting mechanism of CVTM [16–18].

In this study, first, the softening–melting behaviors of chromium-bearing vanadium titanomagnetite pellets (CVTP) with NiO additions were investigated. Then, the slag and iron properties were further discussed. These results will provide theoretical and technical basis for the production of CVTP and other Ni-bearing minerals to produce ferronickel.

2 Experimental

2.1 Raw materials and preparation

The CVTM was derived from the Hongge (Sichuan, China). The chemical compositions of the CVTM and bentonite are listed in Table 1. The ash compositions and fixed carbon of coke used for the smelting of CVTP are shown in Table 1. Figure 1 shows the XRD pattern of the CVTM. The chief minerals of the CVTM are Fe₃O₄, FeTiO₃, and FeCr₂O₄. The analytical grade NiO was purchased from Sinopharm Chemical Reagent Co., Ltd., China.

2.2 Softening–melting treatment

Figure 2(a) shows the equipment diagram of softening–melting treatment. The equipment consists of a heating furnace, automatic control system, and data recording system. The experimental CVTP burden was tested in the graphite crucible (95 mm in outer diameter (O.D); 85 mm in inner diameter (I.D); 250 mm in height) with 15 holes in the bottom to assure the mixed gas through the CVTP effectively and ensure the generated molten iron and primary slag dripping down from the graphite crucible. To imitate the smelting conditions of the BF, first, 47 g coke (10–12.5 mm) was put into the base of the crucible. Then, 500 g pellets were placed above the underlying coke to form a burden layer. Finally, the

Table 1 Chemical compositions of raw materials (wt.%)

Sample	TFe	FeO	TiO ₂	NiO	V ₂ O ₅	Cr ₂ O ₃	CaO	SiO ₂	MgO	Al ₂ O ₃	P	S	C-Fix
CVTM	53.35	26.91	11.60	0.06	0.57	0.81	0.96	4.71	3.33	2.82	0.02	0.26	–
Bentonite	–	–	–	–	–	–	2.19	68.28	3.56	13.45	–	–	–
Coke	–	–	–	–	–	–	2.16	52.71	0.76	29.09	0.25	–	85.5

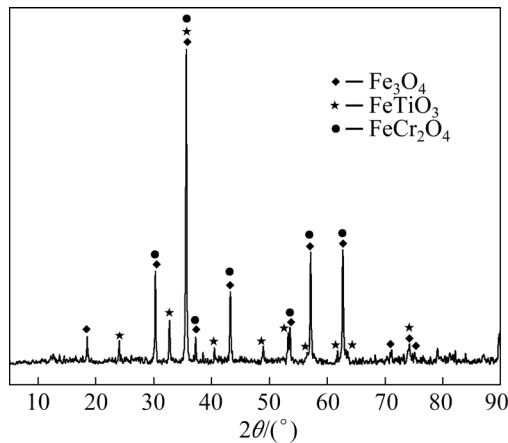


Fig. 1 XRD pattern of CVTM

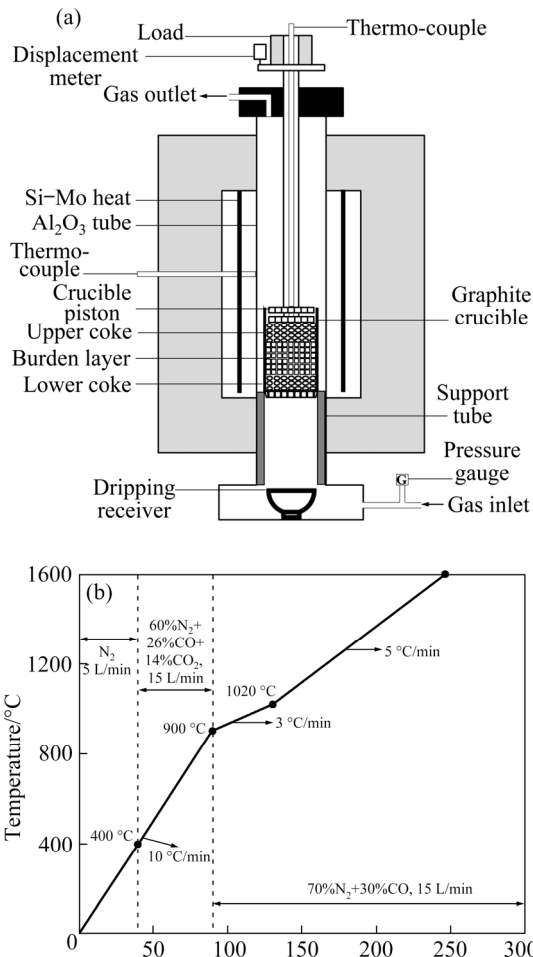


Fig. 2 Softening-melting treatment of CVTP: (a) Equipment diagram; (b) Temperature curve

70 g coke (10–12.5 mm) was tiled above the pellets. In order to gather the molten iron and primary slag from the smelting process, a graphite crucible (95 mm in O.D., 90 mm in I.D., and 80 mm in depth) was placed below the furnace. The temperature in the smelting process was monitored

by an S-type thermocouple. The pressure lever with the graphite rod was inflicted on the upper coke. In the smelting process, the displacement sensor could successively record the displacement mutations of the burden.

Figure 2(b) shows the temperature curve of the softening-melting experiment, and the specific parameters are in the curve. In this study, softening start temperature ($T_{10\%}$) and softening end temperature ($T_{40\%}$) are the temperatures when shrinkage percentages (variation of the displacement sensor/original height of burden) of pellet reach 10% and 40%, respectively. The melting start temperature (T_S) is the temperature that the gas pressure drop begins to increase sharply. The melting end temperature (T_D) is the dripping temperature of the molten iron. The softening zone is the temperature interval ($T_{40\%}-T_{10\%}$). The melting zone is the temperature interval (T_D-T_S).

2.3 Analytical methods

X-ray fluorescence (XRF, ZSXPrimus II; Rigaku, Japan) was used to test the chemical compositions of raw materials, slag, and pig iron. X-ray diffraction (XRD, X' Pert Pro; PANalytical, Almelo, Netherlands) with Cu K α radiation (wavelength = 1.5406 Å) was utilized to detect the phases of CVTM and slag. The scanned range of XRD was $2\theta=5^\circ-90^\circ$ with a step of 0.17° and 1s/step. A scanning electron microscope (SEM, Ultra Plus; Carl Zeiss GmbH, Jena, Germany) was employed to explore the microstructure of slag and pig iron with backscattering detector (BSE) and energy disperse spectroscopy (EDS).

3 Results and discussion

3.1 Softening and melting of CVTP

Figure 3 displays the effect of NiO addition on the softening-melting behaviors of CVTP. The softening start temperature ($T_{10\%}$) increases from 1148 to 1212 °C, and the softening end temperature ($T_{40\%}$) increases from 1280 to 1334 °C. Further, the softening interval ($T_{40\%}-T_{10\%}$) narrows from 132 to 122 °C with the increase in NiO additions. The variation trend is favorable to the stability of BF and gas-solid reduction of pellets. CHENG et al [19] observed that initial reduction of Ti-bearing pellets was restrained due to the difficult reduced iron-titanium oxides. The melting start

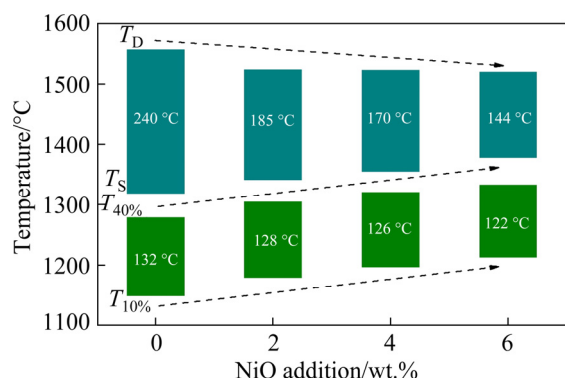


Fig. 3 Softening-melting behaviors of CVTP with NiO additions

temperature (T_S) increases from 1318 to 1377 °C, and the dripping temperature (T_D) decreases from 1558 to 1521 °C. Further, the melting interval ($T_D - T_S$) narrows from 240 to 144 °C with the increase in NiO additions, indicating the decrease of melting-down temperature. Therefore, the softening-melting behaviors of the CVTP are improved, and the cohesive zone moves down and shrinks with the increase in NiO additions, thereby leading to performance improvement of the cohesive zone. The higher softening temperature and shrunken cohesive zone of burden are beneficial in the production of BF [20].

Softening-melting behaviors are usually influenced by the properties of slag and iron. NiO activity is low in slag at ferronickel smelting [21]. BUNJAKU et al [22] explored the existence of Fe–Ni alloy particles in Mg–Fe silicates, demonstrating that the dissolution of nickel in iron silicate phase and wüstite phase hinders the nickel recovery [23]. BRILLO and EGRY [24] indicated that the surface tension of Fe–Ni melt decreases with increasing nickel content. Additionally, the surface tension of Fe–Ni melt reduces with increasing temperature [25]. SATO et al [26] found that the viscosity and activation energy of Fe–Ni melt decrease with increasing nickel content and temperature. The variation tendency of the viscosity of Fe–Ni melts corresponds with the low viscosity and melting point of nickel. Finally, the Fe–Ni melt was a regular solution and had no distinct interactions through the phase diagram. The [Ni] decreases the solubility of carbon in Fe–Ni–C system [27].

3.2 Slag and iron properties

To elucidate the slag and iron properties by

which the NiO additions affect the smelting behavior of CVTP, the XRF, XRD, SEM-EDS, and FT-IR spectroscopy were used to detect and analyze the slag and pig iron samples. The chemical compositions of slag and pig iron are listed in Tables 2 and 3, respectively.

Table 2 Chemical compositions of slag with NiO additions (wt.%)

NiO	FeO	NiO	TiO ₂	CaO	SiO ₂	MgO	Al ₂ O ₃
0	1.65	0.13	36.02	6.61	28.82	12.39	13.48
2	2.74	0.51	35.72	5.65	29.14	12.67	13.36
4	3.21	0.69	36.54	5.51	28.24	12.58	13.31
6	3.59	0.80	37.40	5.37	27.08	12.54	13.28

Table 3 Chemical compositions of pig iron with NiO additions (wt.%)

NiO	Ni	C	Si	V	Cr	Ti	P	S
0	0.40	4.71	0.059	0.161	0.51	0.029	0.020	0.070
2	3.30	4.39	0.040	0.076	0.26	0.014	0.027	0.056
4	5.41	4.42	0.024	0.071	0.21	0.011	0.024	0.057
6	8.29	4.49	0.011	0.063	0.18	0.009	0.022	0.056

The XRD patterns of slag are shown in Fig. 4. It can be observed that the primary phases of slag are MgSiO₃, MgTi₂O₅, and Fe_{0.5}Mg_{0.5}Ti₂O₅. The peak intensities of MgSiO₃ and MgTi₂O₅ occur with no significant change with the increase in NiO additions. The peak intensity of Fe_{0.5}Mg_{0.5}Ti₂O₅ increases slightly due to the increasing amount of iron element in slag.

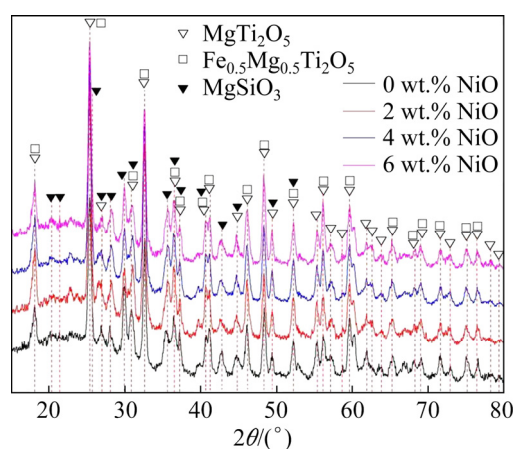


Fig. 4 XRD patterns of slag

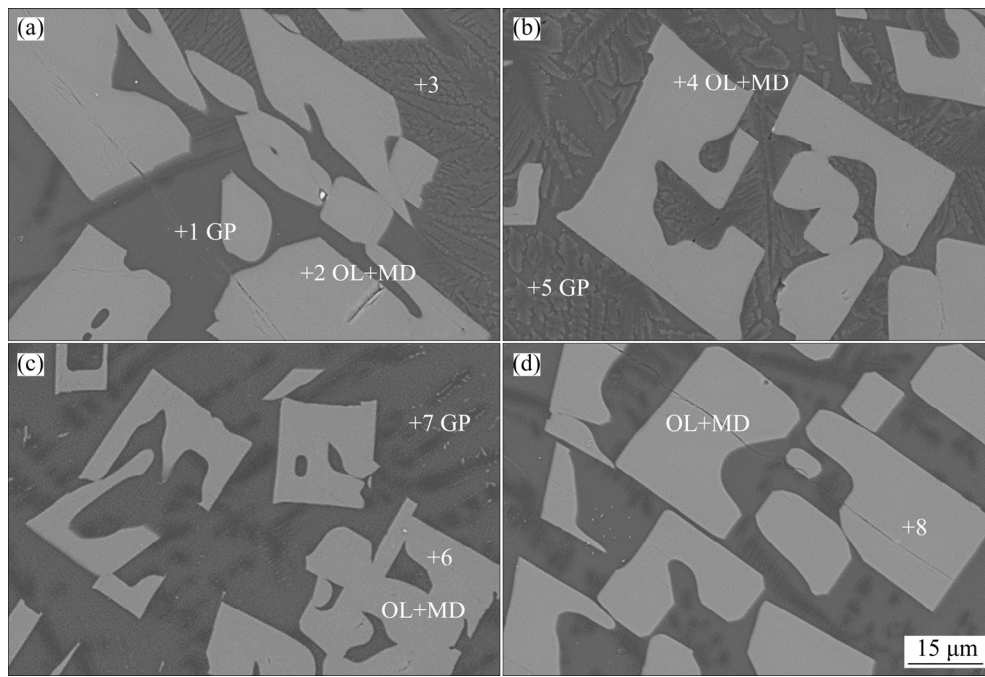
Figure 5 shows the microstructure of slag detected by SEM with variable NiO additions.

Based on the XRD analysis of slag, the main phases of slag are MgTi_2O_5 and MgSiO_3 . As shown in Figs. 5(b)–(d), the MgTi_2O_5 phase is crystallized in the form of bright gray crystals in the slag, while the MgSiO_3 exists as the gray glass phase in the slag. Moreover, a little olkhonskite phase is crystallized in MgTi_2O_5 phase. Additionally, the remanent Ni element is retained in glass phases in the EDS analysis results.

The X-ray elemental mapping of slag with 6 wt.% NiO addition of CVTP pellet is shown in Fig. 6. Figure 6 shows the concentration degree of calcium, aluminum, silicon, titanium, and magnesium in the microstructure of slag. Calcium, aluminum, and silicon are concentrated in a gray structure, and a large proportion of magnesium is

concentrated in a dark gray structure during the glass phase, while magnesium is segregated from calcium and aluminum. In contrast with the above elements, titanium is concentrated in a light color structure with remanent magnesium.

Figure 7 shows the BSE cross-sectional image of slag and neighbor pig iron. The light structure is the Fe–Ni-bearing pig iron, and the other portions of the structure are slag and two-layer intermediate reactants at the interface of slag and metal. From the concentration variation curve in BSE image, the pig iron comprises iron, nickel, and little carbon and chromium. On the next layer of pig iron, the light and thin layer comprises vanadium, chromium, and carbon. In the adjacent thin layer, the bright gray layer mainly comprises titanium, and the



Point No.	Content/wt.%						
	Mg	Al	Si	Ca	Ti	Ni	V
1	9.39	11.06	23.98	8.26	2.52	0.07	0
2	2.82	2.25	0.02	0.15	61.17	0	0.83
3	12.03	11.02	23.81	7.33	2.76	0	0.05
4	3.01	2.24	0.1	0.1	59.68	0	1.03
5	3.47	15.74	27.5	8.69	1.79	0.03	0
6	3.21	2.35	0.09	0.06	59.91	0	1.26
7	24.32	5.21	20.41	2.61	1.54	0.04	0
8	3.51	2.65	0.11	0.08	60.12	0	1.81
9	26.51	4.48	21.91	2.45	1.96	0.07	0

Fig. 5 BSE images and EDS analysis of slag with NiO additions: (a) 0 wt.%; (b) 2 wt.%; (c) 4 wt.%; (d) 6 wt.% (OL: Olkhonskite; MD: magnesium dititanate; GP: Glass phase)

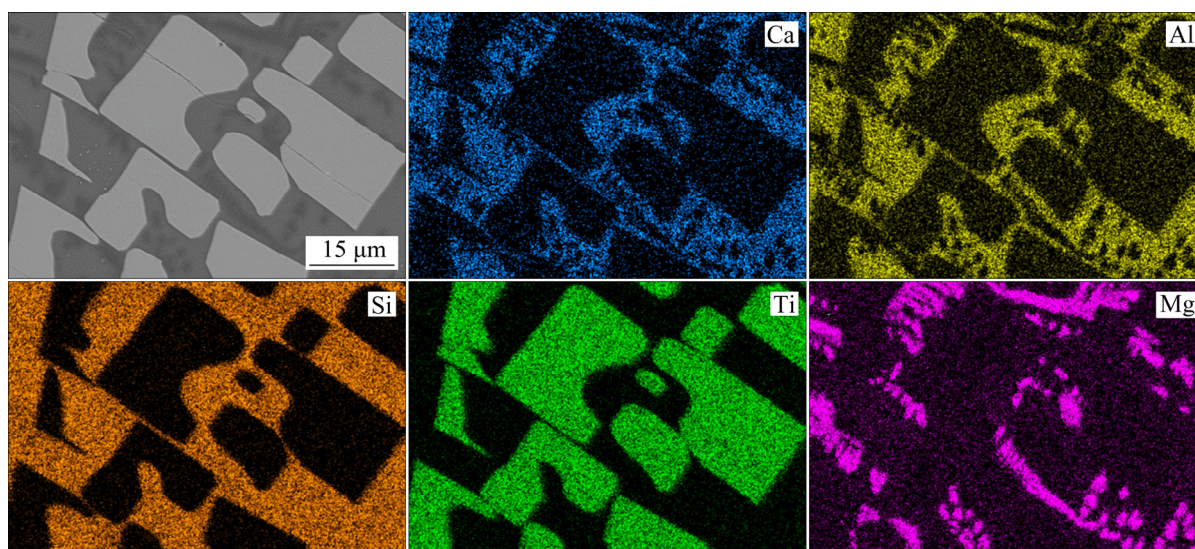
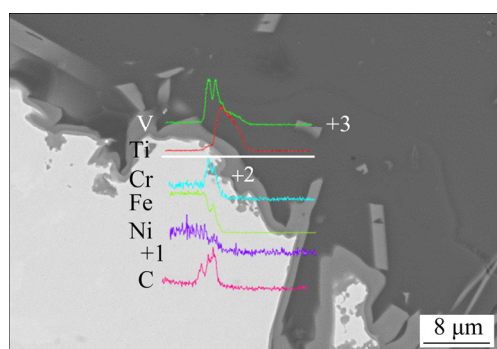


Fig. 6 X-ray element mapping of slag with 6 wt.% NiO addition



Point	Content/wt.%				
	C	Fe	Ni	V	Cr
1	3.71	89.2	3.74	0.27	0.7
2	4.65	1.11	0	0.55	0
3	4.13	0.58	0.05	0.13	0.12
Point	Si	Ca	Ti	Al	Mg
1	0.21	0.02	0.24	0.23	0
2	6.14	2.03	40.47	4.52	4.13
3	23.82	8.97	1.88	12.36	4.63

Fig. 7 BSE cross-sectional image and EDS analysis of slag (light grey and dark gray areas) and neighbor pig iron (bright white area) with 6 wt.% NiO addition

outermost layer comprises slag. With the EDS analysis results of three-pointed phase on Fig. 7, nickel and chromium are concentrated in the pig iron, whereas vanadium is gathered in titanium, which is shown in points 1 and 2 of Fig. 7, respectively. Most of the chromium oxide is reduced to pig iron while it has a low concentration in slag. The overwhelming majority of titanium and

vanadium are found in the intermediate reactant between pig iron and slag. AZOF et al [28] viewed titanium and vanadium as the carbide-forming elements. The trace elements including silicon, calcium, titanium, and aluminum are also detected in pig iron while barely present in intermediate reactant and slag. Additionally, X-ray element mapping of slag and neighbor pig iron in Fig. 8 shows the distribution and concentration of primary elements, and the boundaries of elements reveal the reaction mechanism and coexisting phases in the reduction process. The iron, nickel, and chromium are easier to reduce and concentrate in the reduction process. The titanium, vanadium, and carbon are combined in the reaction layer to generate (Ti,V)C. The EDS analysis results in Figs. 7 and 9 illustrate that titanium is mainly distributed in the intermediate reactant, and the remanent trace titanium exists in pig iron and slag, respectively. The Ti activity is low in the molten iron, and a small degree of reduction of titanium oxide might occur due to the high reduction temperature of titanium oxide. With the addition of coke reaction, the pig iron was carbon saturated, and the dissolved vanadium and titanium have a high probability of combining with dissolved carbon and generating (Ti,V)C in the solidification process. The (Ti,V)C formation is detected in the gray stripe displayed in Fig. 9.

When the titanium content is greater than 0.01 wt.%, the more quantity and possibility of titanium carbide phase will generate at the interface

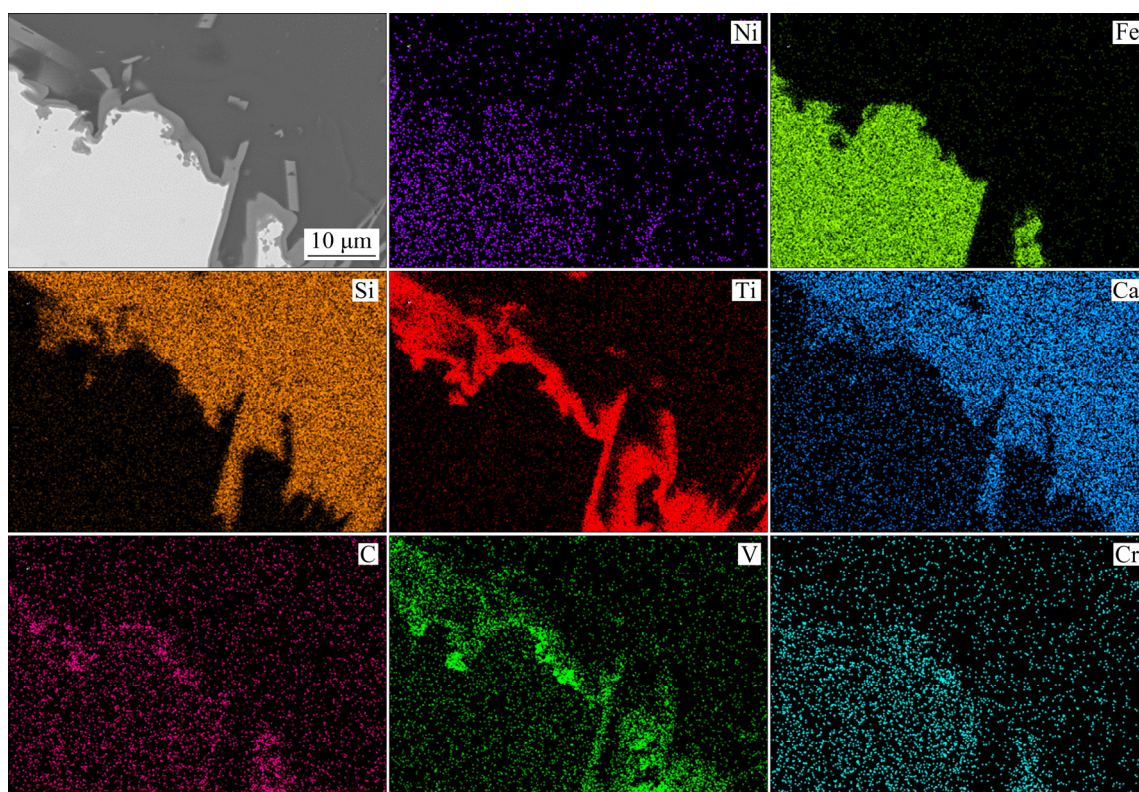
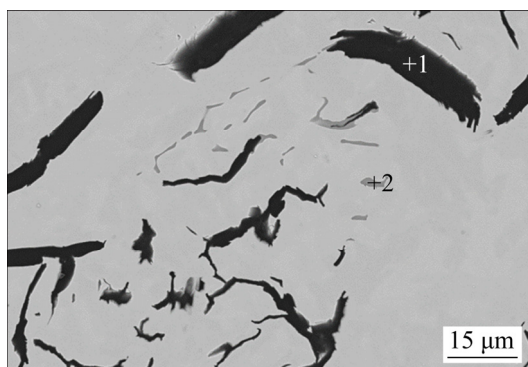


Fig. 8 X-ray element mapping of slag (light grey and dark grey areas) and neighbor pig iron (bright white area) with 6 wt.% NiO addition



Point	Content/wt.%				
	C	O	Fe	Ni	Si
1	94.66	2.97	1.77	0.03	0.03
2	14.06	0.95	5.5	0	0.06

Point	Content/wt.%					
	Ca	Ti	Al	Mg	V	Cr
1	0.13	0.05	0.05	0.07	0.05	0
2	0	70.98	0.11	0	7.68	0.41

Fig. 9 BSE image of neighbor pig iron with 6 wt.% NiO addition

of slag and metal [28]. The X-ray mapping of slag and neighbor pig iron in Fig. 8 and EDS analysis results in Figs. 7 and 9 demonstrate the generation

of (Ti,V)C precipitates in pig iron and interface of pig iron. The solute vanadium and titanium in metal iron might transfer to the interface of pig iron in the form of (Ti,V)C carbide because the solidus temperature of the metal is lower than that of slag.

The slags are acidic because the binary basicities of slags are around 0.2. From the viscosity curve calculated by FactSage 7.0 in Fig. 10, the melting temperatures decrease from 1356 to 1304 °C (green icon in Fig. 10) with the original compositions of smelting slag. Although the TiO₂ content increases in slag, the melting temperatures of slag are reduced due to the destructive effect of Ti⁴⁺ on the Si—O—Ti ionic group. Hence, the complicated Si—O ionic group is transformed to a simple structure, contributing to the decrease of slag viscosity.

FT-IR spectroscopy is utilized to characterize the structures of slag, as shown in Fig. 11. Four major peaks for Si—O bonds are defined as sheets (1100–1050 cm⁻¹), chains (980–950 cm⁻¹), polyhedra (920–900 cm⁻¹) and monomers (880–850 cm⁻¹) which are assigned to NBO/Si=1, 2, 3, and 4, respectively [29–31]. The band groups at 720–630 and 570–520 cm⁻¹ correspond to the

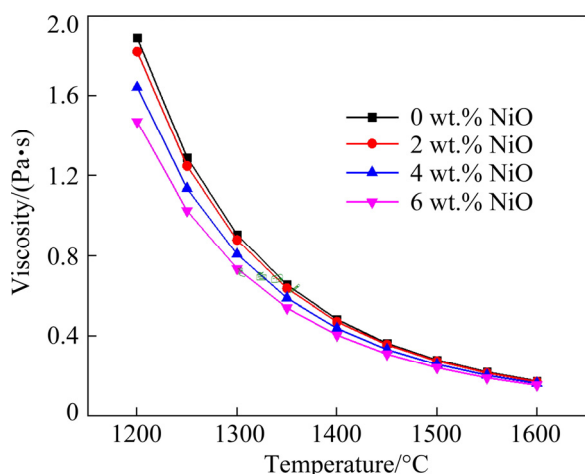


Fig. 10 FactSage7.0 results for viscosity of slag in Table 2

$[\text{AlO}_4]$ tetrahedrons and $[\text{AlO}_6]$ octahedrons, respectively [32,33]. The band group near 500 cm^{-1} corresponds to the $[\text{Si}-\text{O}-\text{Al}]$ bending band. The chemical compositions of slag show that the main compositions are TiO_2 , SiO_2 , and Al_2O_3 . The obvious change of slag composition is the FeO content, which changes from 1.65 to 3.59 wt.%, and the NiO content increases from 0.13% to 0.80 wt.%. The depths of the $[\text{SiO}_4]$ tetrahedra become shallow. The decreasing depth of the $[\text{SiO}_4]$ tetrahedra shows depolymerization of slag structure [34]. The decreased depth of the $[\text{Si}-\text{O}-\text{Al}]$ bending band at 473.6 cm^{-1} indicates that the slag is depolymerized. The slightly increased depth of the $[\text{AlO}_4]$ tetrahedrons at 669 cm^{-1} demonstrates that there is virtually no variation of the band on the slag.

Therefore, the Ti-bearing slag is depolymerized with the dissociated effect of Ti^{4+} on the $[\text{SiO}_4]$ tetrahedra due to the TiO_2 as basic oxide and network modifiers. JIAO et al [35] reported that the slag viscosity decreases with enhance stretch vibration of $\text{O}-\text{Ti}-\text{O}$ and $\text{O}-(\text{Si},\text{Ti})-\text{O}$, and increasing TiO_2 content in BF primary slag.

3.3 Elements migration between slag and iron

Based on the EDS analysis and XRF results of pig iron, the main compositions are Fe, Ni, and C. The vast majority of Cr is also reduced in pig iron. The other phase such as $(\text{Ti},\text{V})\text{C}$ is related to the elemental distributions in the smelting and cooling process. The X-ray mapping results of slag and neighbor pig iron illustrate the low activity of vanadium and titanium in pig iron. In the carbon reduction condition, the reductive vanadium and titanium are likely to react with carbon to generate TiC and VC . Hence, the generation of TiC and VC further decreases the solubility of vanadium and titanium in pig iron. FU et al [36] studied the generation mechanism of $(\text{Ti},\text{V})\text{C}$ in the Fe-Ti-V-C system, and the four parts of reaction mechanism including the generation of VC at $756.7\text{ }^\circ\text{C}$ between FeV and C, Fe_2Ti at $1058.5\text{ }^\circ\text{C}$ with eutectic reaction of Ti and Fe, TiC at $1140.4\text{ }^\circ\text{C}$ between Fe_2Ti and C, and $(\text{Ti},\text{V})\text{C}$ with solubility of TiC and VC . WANG et al [37] examined the reaction composition of Fe and $(\text{Ti},\text{V})\text{C}$ with different V/Ti ratios, and the VC with higher density reacted with titanium to generate $(\text{Ti},\text{V})\text{C}$.

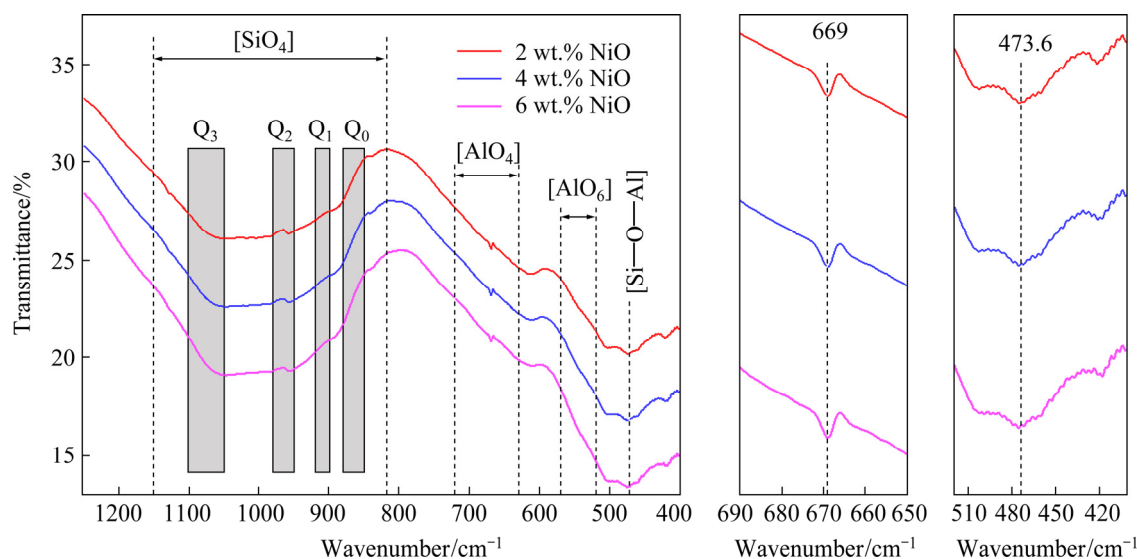


Fig. 11 FT-IR spectroscopy results of slag

4 Conclusions

(1) The decreasing trends of softening interval ($T_{40\%}-T_{10\%}$) and melting interval (T_D-T_S) indicate the improving softening-melting behaviors and cohesive zone performance.

(2) The primary phases of slag are $MgSiO_3$, $MgTi_2O_5$, and $Fe_{0.5}Mg_{0.5}Ti_2O_5$. The (Ti,V)C as intermediate reactant generates precipitates in pig iron and the interface of pig iron.

(3) From the viscosity curve calculated by FactSage 7.0, the melting temperatures decrease from 1356 to 1304 °C with the original compositions of smelting slag. The depolymerization of slag results in low viscosity of slag, leading to the performance improvement of the softening-melting behaviors. The results indicate that nickel-iron alloy can be manufactured by the blast furnace process.

Acknowledgments

The authors are grateful for the financial supports from the National Natural Science Foundation of China (Nos. 21908020, U1908226).

References

- [1] TAKANO C, ZAMBRANO A P, NOGUEIRA A E A, MOURAO M B, IGUCHI Y. Chromites reduction reaction mechanisms in carbon-chromites composite agglomerates at 1773 K [J]. ISIJ International, 2007, 47(11): 1585–1589.
- [2] LU Chang-yuan, ZOU Xing-li, LU Xiong-gang, XIE Xue-liang, ZHENG Kai, XIAO Wei, CHENG Hong-wei, LI Guang-shi. Reductive kinetics of Panzhihua ilmenite with hydrogen [J]. Transactions of Nonferrous Metals Society of China, 2016, 26(12): 3266–3273.
- [3] LI Guang-hui, JIA Hao, LUO Jun, PENG Zhi-wei, ZHANG Yuan-bo, JIANG Tao. Characterization of minerals, metals, and materials [M]. Cham: Springer, 2016.
- [4] DENNIS W H. Metallurgy of the non-ferrous metals [M]. London: Pitman, 1966.
- [5] BERGMAN R A. Nickel production from low-iron laterite ores: Process descriptions [J]. CIM Bulletin, 2003, 96(1072): 127–138.
- [6] ELLIOTT R, PICKLES C A, PEACEY J. Ferronickel particle formation during the carbothermic reduction of a limonitic laterite ore [J]. Minerals Engineering, 2017, 100: 166–176.
- [7] LI Bo, WANG Hua, WEI Yong-gang. The reduction of nickel from low-grade nickel laterite ore using a solid-state deoxidation method [J]. Minerals Engineering, 2011, 24(14): 1556–1562.
- [8] ZHU De-qing, XUE Yu-xiao, PAN Jian, YANG Cong-cong, GUO Zheng-qi, TIAN Hong-yu, LIAO Hui, PAN Liao-ting, HUANG Xue-zhong. An investigation into the distinctive sintering performance and consolidation mechanism of limonitic laterite ore [J]. Powder Technology, 2020, 367: 616–631.
- [9] ZHU De-qing, PAN Liao-ting, GUO Zheng-qi, PAN Jian, ZHANG Fang. Utilization of limonitic nickel laterite to produce ferronickel concentrate by the selective reduction-magnetic separation process [J]. Advanced Powder Technology, 2019, 30(2): 451–460.
- [10] RAO Ming-jun, LI Guang-hui, JIANG Tao, LUO Jun, ZHANG Yuan-bo, FAN Xiao-hui. Carbothermic reduction of nickeliferous laterite ores for nickel pig iron production in China: A review [J]. JOM, 2013, 65(11): 1573–1583.
- [11] ZHOU Shi-wei, WEI Yong-gang, LI Bo, WANG Hua, MA Bao-zhong, WANG Cheng-yan. Chloridization and reduction roasting of high-magnesium low-nickel oxide ore followed by magnetic separation to enrich ferronickel concentrate [J]. Metallurgical and Materials Transactions B, 2015, 47: 145–153.
- [12] LIU Zhi-guo, SUN Ti-chang, WANG Xiao-ping, GAO En-xia. Generation process of FeS and its inhibition mechanism on iron mineral reduction in selective direct reduction of laterite nickel ore [J]. International Journal of Minerals, Metallurgy, and Materials, 2015, 22(9): 901–906.
- [13] TIAN Hong-yu, PAN Jian, ZHU De-qing, YANG Cong-cong, GUO Zheng-qi, XUE Yu-xiao. Improved beneficiation of nickel and iron from a low-grade saprolite laterite by addition of limonitic laterite ore and $CaCO_3$ [J]. Journal of Materials Research and Technology, 2020, 9(2): 2578–2589.
- [14] LI Xiao-ming, WEN Zhen-yu, LI Yi, YANG Hai-bo, XING Xiang-dong. Improvement of carbothermic reduction of nickel slag by addition of $CaCO_3$ [J]. Transactions of Nonferrous Metals Society of China, 2019, 29(12): 2658–2666.
- [15] YUAN Shuai, ZHOU Wen-tao, LI Yan-jun, HAN Yue-xin. Efficient enrichment of nickel and iron in laterite nickel ore by deep reduction and magnetic separation [J]. Transactions of Nonferrous Metals Society of China, 2020, 30(3): 812–822.
- [16] TANG Wei-dong, YANG Song-tao, CHENG Gong-jin, GAO Zi-xian, XUE Xiang-xin. Effect of MgO in sinter and primary-slag on smelting mechanism of chromium-bearing vanadium titanomagnetite [J]. Steel Research International, 2018, 89(11): 1800226.
- [17] TANG Wei-dong, YANG Song-tao, XUE Xiang-xin. Effect of V_2O_5 addition on oxidation induration and swelling behavior of chromium-bearing vanadium titanomagnetite pellets with simulated coke oven gas injection into blast furnace [J]. ISIJ International, 2019, 59(6): 988–997.
- [18] TANG Wei-dong, YANG Song-tao, XUE Xiang-xin. Effect of B_2O_3 addition on oxidation induration and reduction swelling behavior of chromium-bearing vanadium titanomagnetite pellets with simulated coke oven gas [J]. Transactions of Nonferrous Metals Society of China, 2019, 29(7): 1549–1559.
- [19] CHENG Gong-jin, XUE Xiang-xin, JIANG Tao, DUAN Pei-ning. Effect of TiO_2 on the crushing strength and

- smelting mechanism of high-chromium vanadium-titanium magnetite pellets [J]. Metallurgical and Materials Transactions B, 2016, 47: 1713–1726.
- [20] LIU Jian-xing, CHENG Gong-jin, LIU Zheng-gen, CHU Man-sheng, XUE Xiang-xin. Softening and melting properties of different burden structures containing high chromic vanadium titanomagnetite [J]. International Journal of Mineral Processing, 2015, 142: 113–118.
- [21] SWINBOURNE D R. Understanding ferronickel smelting from laterites through computational thermodynamics modelling [J]. Mineral Processing and Extractive Metallurgy, 2014, 123(3): 127–140.
- [22] BUNJAKU A, KEKKONEN M, TASKINEN P. Effect of mineralogy on reducibility of calcined nickel saprolite ore by hydrogen [J]. Mineral Processing and Extractive Metallurgy, 2013, 121(1): 16–22.
- [23] ELLIOTT R, RODRIGUES F, PICKLES C A, PEACEY J. A two-stage thermal upgrading process for nickeliferous limonitic laterite ores [J]. Canadian Metallurgical Quarterly, 2016, 54(4): 395–405.
- [24] BRILLO J, EGRY I. Surface tension of nickel, copper, iron and their binary alloys [J]. Journal of Materials Science, 2005, 40: 2213–2216.
- [25] KEENE B J. Review of data for the surface tension of iron and its binary alloys [J]. International Materials Reviews, 1988, 33(1): 1–37.
- [26] SATO Y, SUGISAWA K, AOKI D, YAMAMURA T. Viscosities of Fe–Ni, Fe–Co and Ni–Co binary melts [J]. Measurement Science and Technology, 2005, 16: 363–371.
- [27] GABRIEL A, GUSTAFSON P, ANSARA I. A thermodynamic evaluation of the C–Fe–Ni system [J]. Calphad, 1987, 11(2): 203–218.
- [28] AZOF F I, KOLBEINSEN L, SAFARIAN J. Characteristics of calcium–aluminate slags and pig iron produced from smelting-reduction of low-grade bauxites [J]. Metallurgical and Materials Transactions B, 2018, 49: 2400–2420.
- [29] HANDKE M, SITARZ M, MOZGAWA W. Model of silico oxygen ring vibrations [J]. Journal of Molecular Structure, 1998, 450: 229–238.
- [30] SITARZ M, HANDKE M, MOZGAWA W, GALUSKIN E, GALUSKINA I. The non-ring cations influence on silico oxygen ring vibrations [J]. Journal of Molecular Structure, 2000, 555(1): 357–362.
- [31] SITARZ M, HANDKE M, MOZGAWA W. Identification of silico oxygen rings in SiO₂ based on IR spectra [J]. Spectrochimica Acta, Part A, 2000, 56(9): 1819–1823.
- [32] ZIRL D M, GAROFALINI S H. Structure of sodium aluminosilicate glasses [J]. Journal of the American Ceramic Society, 1990, 73(10): 2848–2856.
- [33] TARTEP. Infra-red spectra of inorganic aluminates and characteristic vibrational frequencies of AlO₄ tetrahedra and AlO₆ octahedra [J]. Spectrochimica Acta: Part A, 1967, 23(7): 2127–2143.
- [34] KIM H, KIM W H, SOHN I, MIN D J. The effect of MgO on the viscosity of the CaO–SiO₂–20wt.%Al₂O₃–MgO slag system [J]. Steel Research International, 2010, 81(4): 261–264.
- [35] JIAO Ke-xin, ZHANG Jian-liang, WANG Zhi-yu, CHEN Chun-lin, LIU Yan-xiang. Effect of TiO₂ and FeO on the viscosity and structure of blast furnace primary slags [J]. Steel Research International, 2017, 88(5): 1600296.
- [36] FU S J, CHENG H, YAN Y L, WANG J, DING Y C. Study on Fe–Ti–V–C composite produced by self-propagating high temperature synthesis [J]. Powder Metallurgy, 2009, 52(4): 334–337.
- [37] WANG Jing, WANG Yi-san, DING Yi-chao. Reaction synthesis of Fe–(Ti,V)C composites [J]. Journal of Materials Processing Technology, 2008, 197(1): 54–58.

氧化镍对含铬型钒钛磁铁矿球团冶炼机理的影响

程功金, 汤卫东, 薛向欣

东北大学 冶金学院, 沈阳 110819

摘要: 研究氧化镍对含铬型钒钛磁铁矿球团冶炼行为的影响, 分析镍在铁水和渣间的迁移行为。结果表明, 当含铬型钒钛磁铁矿球团中 NiO 的添加量从 0 提高到 6%(质量分数)时, 软化开始温度从 1148 °C 升高至 1212 °C, 软化结束温度从 1280 °C 升高至 1334 °C; 熔化开始温度从 1318 °C 升高到 1377 °C, 滴落温度从 1558 °C 降低到 1521 °C。生铁是 Fe–Ni–C 的化合物。炉渣结构的解聚程度随含铬型钒钛磁铁矿球团中镍添加量的增加而提高。含铬型钒钛磁铁矿球团的软熔滴落性能、镍的还原以及冶炼过程中炉渣结构的解聚程度表明通过高炉流程生产镍铁合金的可行性。

关键词: 镍铁合金; 含铬型钒钛磁铁矿球团; 冶炼机理; 渣结构

(Edited by Xiang-qun LI)